Origin of space charge in grain boundaries of proton-conducting BaZrO₃

E. E. Helgee[1], A. Lindman[1], and G. Wahnström[1]*

[1] Dept. of Applied Physics, Chalmers University of Technology, SE-412 96, Göteborg, Sweden

[*] Corresponding Author, goran.wahnstrom@chalmers.se

Abstract

Segregation energies of oxygen vacancies and protons near three symmetric tilt grain boundaries in BaZrO₃ are determined using density functional theory. Two of the grain boundaries have the $[\bar{1}10]$ direction as tilt axis with a (111) or (112) plane as grain boundary plane, while the third has the [001] direction as tilt axis and a (210) plane as grain boundary plane. Both defects are found to segregate to all three grain boundaries, with vacancy segregation energies of −0.5 eV and −1.5 eV and proton segregation energies of about −0.8 eV. The effects of the calculated segregation energies on defect concentrations and electrostatic potential in the grain boundary region are investigated using a thermodynamic space charge model. An increased concentration of defects is seen in all grain boundaries, giving electrostatic potential barriers around 0.6 V at 400-600 K. Protons are found to give important contributions to the space charge in all three grain boundaries.

1 Introduction

Acceptor-doped barium zirconate (BaZrO₃) shows considerable potential as an electrolyte material for intermediate-temperature solid oxide fuel cells due to its high bulk proton conductivity and chemical stability [1-3]. However, in polycrystalline materials the grain boundaries display high proton resistivity [1,4-9], severely limiting the overall proton transport in the material. High grain boundary resistance in oxides is often caused by non-conducting phases segregating to the boundaries [10,11], but for barium zirconate that is hardly the case as grain boundaries in BaZrO₃ are clean and show no sign of secondary grain boundary phases [12-14]. The low grain boundary conductivity has therefore been thought to be due to an intrinsic mechanism, and recently the so called space charge model has been used to interpret and explain the grain boundary blocking behaviour in BaZrO₃ by several research groups [14-22].

According to the space charge model, charged defects segregate to the structurally distorted region near the grain boundary plane, the grain boundary core. The resulting core charge gives rise to an electrostatic potential barrier and causes depletion of mobile charge carriers of the same polarity in the regions adjacent to the core, the space charge layers [11,23,24]. Figure 1 gives a schematic view of how concentrations and potential may vary across a grain boundary in acceptor-doped BaZrO₃ according to the space charge model. Several experimental studies have found evidence of space charge layers and a positive core charge in BaZrO₃ [14,15,17-19,21,22]. Impedance spectroscopy is used to determine the grain boundary and bulk conductivities, from which the height of the potential barrier can be derived. Barrier heights of 0.3-0.9 V have been found for dopant contents between 5 and 20 % and are seen to decrease with increasing dopant concentration [17].

The existence of a positive core charge is crucial to the application of the space charge model to BaZrO₃. In a previous study, we used density functional theory (DFT) to investigate oxygen vacancy segregation to a symmetric tilt grain boundary with the $[\bar{1}10]$ direction as rotational axis and a (112) plane as grain boundary plane [20]. We found that oxygen vacancies segregate to the grain boundary and create a positive core charge [20]. Similarly, van Duin et al. found oxygen deficiency and a resulting positive net charge in the core of a twist grain boundary in yttrium-doped BaZrO₃ using molecular dynamics simulations together with a reactive force-field model for the interatomic interaction [25]. Here, we extend our previous study [20] to two other symmetric tilt grain boundaries (GBs), the (111)$[\bar{1}10]$ and the (210)[001]. Segregation energies of both +2 charged oxygen vacancies and +1 charged hydroxide ions are determined and used in a one-dimensional thermodynamic space charge model. Defect concentrations across the grain boundary are calculated, as well as the total charge of the

grain boundary core and the electrostatic potential barrier associated with each grain boundary. All quantities are determined as functions of temperature and both wet and dry conditions are considered.

2 Theory

The purpose of our space charge model is to determine the concentration profiles and electrostatic potential near a grain boundary in acceptor-doped $BaZrO_3$, given that the formation energies of defects in the grain boundary region differ from those in the grain interior. We will assume that the relevant defects are oxygen vacancies, hydroxide ions and acceptor dopants, and that the concentration of electron holes is negligible. Cation vacancies, interstitals and electrons are also not considered. Hydroxide ions and oxygen vacancies are assumed to be mobile while the dopant ions are considered frozen at a uniform concentration. The material is assumed to be in equilibrium with water vapor according to the hydration reaction

$$H_2O(g) + V_O^{\cdot\cdot} + O_O^{\times} \leftrightarrow 2\,OH_O\,. \qquad (1)$$
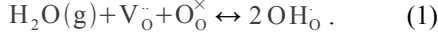
This reaction has the equilibrium constant

$$K_{hydr}(T) = \frac{c_{OH}^2}{c_V c_O p_{H_2O}} = \exp(-\Delta G_{hydr}^o / k_B T)\,, \qquad (2)$$

where $\Delta G_{hydr}^o = \Delta H_{hydr}^o - T \Delta S_{hydr}^o$ is the Gibbs free energy of hydration, c_V the concentration of oxygen vacancies, c_{OH} the concentration of hydroxide ions, c_O the concentration of oxygen ions and p_{H_2O} the water vapor partial pressure. Every site in the anion sublattice can either be vacant or occupied by an oxygen or hydroxide ion. There are three anion sites per formula unit, which gives the site restriction

$$c_V + c_O + c_{OH} = 3\,. \qquad (3)$$

Charge neutrality requires that

$$2 c_V + c_{OH} = c_A\,, \qquad (4)$$

where c_A is the concentration of trivalent dopant atoms at Zr sites (effective charge -1). Combining these equations and solving for c_V and c_{OH} gives

$$c_{OH} = \frac{3\kappa}{\kappa - 4}\left[1 - \sqrt{1 - \frac{\kappa - 4}{3\kappa} c_A \left(2 - \frac{c_A}{3}\right)}\right] \qquad (5)$$

and

$$c_V = \frac{1}{2}(c_A - c_{OH})\,, \qquad (6)$$

where we have used the notation $\kappa = p_{H_2O} K_{hydr}(T)$.

Close to a grain boundary the local concentration of defects may differ from the grain interior value and depend on the distance to the grain boundary. Let the model be one-dimensional and take the grain boundary plane to be situated at $z=0$. The probability that an arbitrary oxygen site i at position z is vacant is then given by

$$P_V^i = \frac{\exp([\mu_V - (E_V^i + 2e\varphi(z))]/k_B T)}{1 + \exp([\mu_V - (E_V^i + 2e\varphi(z))]/k_B T) + \exp([\mu_{OH} - (E_{OH}^i + e\varphi(z))]/k_B T)} \qquad (7)$$

where $E_{V,OH}^i$ is the energy of a defect at the given site, $\mu_{V,OH}$ is the chemical potential of a defect and φ is the electrostatic potential. A corresponding expression is valid for P_{OH}^i. Far away from the grain boundary, in the grain interior, we assume the constant values $E_V^i = E_V^{gi}$, $E_{OH}^i = E_{OH}^{gi}$ and $\varphi(z) = \varphi(\infty)$. The chemical potentials can then be expressed as

$$\mu_V = E_V^{gi} + 2e\varphi(\infty) + k_B T \ln\left(\frac{c_V}{3 - c_{OH} - c_V}\right) \qquad (8)$$

$$\mu_{OH} = E_{OH}^{gi} + e\varphi(\infty) + k_B T \ln\left(\frac{c_{OH}}{3 - c_V - c_{OH}}\right)\,, \qquad (9)$$

where c_V and c_{OH} are given by Eqs. (5) and (6). Implicit in Eqs. (8) and (9) is the assumption that the grain interior is large compared to the grain boundary region and acts as a thermodynamic reservoir.

Defining the defect segregation energies $\Delta E_V^i = E_V^i - E_V^{gi}$ and $\Delta E_{OH}^i = E_{OH}^i - E_{OH}^{gi}$ and expressing the difference in electrostatic potential as $\Delta\varphi(z) = \varphi(z) - \varphi(\infty)$ we can now write

$$P_V^i = \frac{c_V \exp(-(\Delta E_V^i + 2e\Delta\varphi(z))/k_B T)}{3 + c_V[\exp(-(\Delta E_V^i + 2e\Delta\varphi(z))/k_B T) - 1] + c_{OH}[\exp(-(\Delta E_{OH}^i + e\Delta\varphi(z))/k_B T) - 1]} \qquad (10)$$

$$P_{\mathrm{OH}}^i = \frac{c_{\mathrm{OH}}\exp\left(-(\Delta E_{\mathrm{OH}}^i + e\,\Delta\varphi(z))/k_{\mathrm{B}}T\right)}{3 + c_{\mathrm{V}}\left[\exp\left(-(\Delta E_{\mathrm{V}}^i + 2\,e\,\Delta\varphi(z))/k_{\mathrm{B}}T\right)-1\right] + c_{\mathrm{OH}}\left[\exp\left(-(\Delta E_{\mathrm{OH}}^i + e\,\Delta\varphi(z))/k_{\mathrm{B}}T\right)-1\right]} \quad (11)$$

assuming equilibrium between defects in the grain interior and grain boundary region. We characterize the defect state with a single energy value $E_{\mathrm{V,OH}}^i$. In general, several energy values should be considered leading to inclusion of e.g. non-configurational contributions to the entropy. However, to a first approximation these effects are similar for defects located in the grain boundary or grain interior region and the energy differences $\Delta E_{\mathrm{V,OH}}^i$, the segregation energies, should therefore capture the most important contribution.

In a typical grain boundary, defects situated at the same distance from the grain boundary may have different segregation energies. To obtain the defect concentrations as a function of z we use a layer-by-layer approach and model the grain boundary as a stack of layers in the z direction. Each layer is electrically neutral in the absence of defects and contains a number N_{L} of oxygen sites that may have different segregation energies for the two considered defects. The defect concentration is obtained as an average over the different sites:

$$c_{\mathrm{V}}(z) = \frac{3}{N_{\mathrm{L}}}\sum_{i=1}^{N_{\mathrm{L}}} P_{\mathrm{V}}^i \quad (12)$$

and

$$c_{\mathrm{OH}}(z) = \frac{3}{N_{\mathrm{L}}}\sum_{i=1}^{N_{\mathrm{L}}} P_{\mathrm{OH}}^i . \quad (13)$$

For large distances the concentrations should approach the grain interior values, $c_{\mathrm{V,OH}}(z=\infty)=c_{\mathrm{V,OH}}$. We can now introduce the layer volume $V_{\mathrm{L}}(z)$ and obtain the charge density as

$$\rho(z) = \frac{e}{V_{\mathrm{L}}(z)}\left[2c_{\mathrm{V}}(z) + c_{\mathrm{OH}}(z) - c_{\mathrm{A}}\right] \quad (14)$$

The potential can then be obtained from Poisson's equation

$$\frac{\mathrm{d}^2\varphi(z)}{\mathrm{d}z^2} = -\frac{1}{\varepsilon_0\varepsilon_{\mathrm{r}}}\rho(z) \quad (15)$$

where ε_{r} is the relative dielectric constant.

3 Method

3.1 First-principles Calculations

The first-principles calculations have been performed within the framework of density functional theory (DFT) using the program package VASP (version 5.2) which employs a plane-wave basis set [26,27]. The generalized gradient PBE functional [28] is used to approximate exchange and correlation and the projector-augmented wave method (PAW) [29] is used to describe the ion-electron interaction. The explicitly treated valence states are (5s, 5p, 6s) for Ba, (4s, 4p, 5s, 4d) for Zr, (2s, 2p) for O and (1s) for H. All calculations are performed non-spin polarized [30,31] and periodic boundary conditions are used in all three directions.

The k-point sampling has been performed with a Monkhorst-Pack grid, containing $2\times4\times1$ grid points for the $(111)[\bar{1}10]$ and $(112)[\bar{1}10]$ GBs. For the $(210)[001]$ GB, $3\times3\times1$ grid points are used for the smaller supercells and $2\times2\times1$ grid points for the larger. The RMM-DIIS method is employed for ionic relaxation, and the simulations are considered to be converged when the residual forces are smaller than 0.03 eV/Å. A cutoff energy of 470 eV is used when the supercell size is fixed, while simulations where the supercell size is allowed to vary require a cutoff of 600 eV. When charged defects such as oxygen vacancies and interstitial protons are considered electrons are removed from the cell in order to create the appropriate charge state. The resulting net charge of the cell is compensated by a homogeneous background charge of the same magnitude but with opposite sign. Only +2 charged oxygen vacancies are considered as previous studies find this to be the most energetically favourable charge state in the bulk material [30].

The considered grain boundaries are all stochiometric, symmetric tilt grain boundaries. Compared to the minimum supercell size required by the lattice periodicity, the supercells of the $(111)[\bar{1}10]$ and $(112)[\bar{1}10]$ GBs have been enlarged by a factor of two in the $[\bar{1}10]$ direction in order to allow for sufficient ionic relaxation. Likewise, the $(210)[001]$ GB has been enlarged in the $[001]$ direction by a factor of three in calculations with vacancies and by a factor of two in calculations with protons. Size and orientation of the considered supercells can be seen in Table 1.

With regard to the grain boundary structure, only mirror-symmetric configurations have been considered. For each grain boundary, there exists two mirror symmetric configurations with different termination (different elements in the grain boundary plane). The termination which yields the lowest grain boundary energy has been chosen in each case. Figures 2-4 show the structures of the considered grain boundaries.

3.2   Space Charge Modelling

A layer-by-layer approach is used to determine the defect concentrations and electrostatic potential close to the grain boundary plane. Each layer is chosen so that it is charge neutral in the defect free case. For the layers closest to the grain boundary plane ($|z|<z_c$, the "core", cf. Fig. 1) we assume a finite segregation energy for oxygen vacancies and protons. Further away from the grain bondary plane ($z_c<|z|<z_{max}$, the "space charge layers", cf. Fig. 1) the segregation energies will be set equal to zero while the electrostatic potential may differ from the bulk value, so that $\Delta\varphi(z)\neq0$. At $|z|=z_{max}$ the defect concentration is set equal to the bulk values and $\Delta\varphi(|z|=z_{max})=0$. Furthermore, we have the boundary condition $\Delta\varphi'(|z|=z_{max})=0$ which ensures that the region $|z|<z_{max}$ is charge neutral.

Equations (10)-(11) which define the defect concentrations and equations (14)-(15) which define the potential are solved iteratively. Poisson's equation (15) is solved using the Jacobi method [32], after which concentrations are calculated from (10)-(11) using the resulting potential. The new concentrations yield a new charge density according to (14), and the procedure is repeated until the concentrations and potential have converged to their equilibrium profiles. Further details on the computational method can be found in Ref. [33].

The concentration of hydroxide ions in the material depends on the water partial pressure and the hydration enthalpy and entropy according to Eq. (5). For the water partial pressure we use $p_{H_2O}=0.025$ bar. Following experimental results the hydration enthalpy is taken to be $\Delta H_{hydr}^o=-0.82$ eV and the hydration entropy $\Delta S_{hydr}^o=-0.92$ meVK^{-1} [1]. The dopant concentration is set to a constant value of 10 site % across the grain boundary region, $c_A=0.1$. Concentrations of oxygen vacancies and hydroxide ions in bulk under these conditions can be seen in Figure 5.

The relative dielectric constant ε_r is taken to be constant across the grain boundary region and is assumed independent of temperature. A value of $\varepsilon_r=75$ has been chosen in accordance with experimental data [17].

4 Results and Discussion
4.1   DFT Calculations

First we consider grain boundaries (GBs) without defects. Each grain boundary is associated with a grain boundary energy defined as

$$\gamma_{gb}=\frac{E_{gb}^{tot}-E_{bulk}^{tot}}{2A}, \quad (16)$$

where E_{gb}^{tot} is the total energy of the supercell with grain boundary, E_{bulk}^{tot} is the total energy of a supercell of the same size and orientation but without grain boundary, and A is the grain boundary area. The factor of two is included since each supercell contains two identical grain boundaries. The same cutoff energy and k-point sampling were used for the bulk and grain boundary supercells. Around the grain boundary the stucture of the material is distorted. To accomodate these distortions, supercells containing grain boundaries are allowed to change size in the direction perpendicular to the grain boundary during the ionic relaxation. This results in a grain boundary expansion Δ_{gb} which is defined as the difference in length between the grain boundary supercell and the corresponding bulk supercell, divided by two.

Grain boundary (GB) energies and expansions can be seen in Table 2. The $(111)[\bar{1}10]$ GB is the most stable with a grain boundary energy of 0.51Jm^{-2}, while the $(112)[\bar{1}10]$ GB has the smallest expansion, 0.14 Å. The (210)[001] GB has both the highest grain boundary energy and the largest expansion.

Next, we consider grain boundaries with defects. The segregation energy of a defect can be written

$$\Delta E_D=E_{gb,D}^{tot}-E_{gb,Dref}^{tot} \quad (17)$$

where $E_{gb,D}^{tot}$ is the total energy of the supercell with the considered defect and $E_{gb,Dref}^{tot}$ is the total energy of a supercell containing a defect in a reference state. The subscript D stands for either a vacancy (V) or a hydroxide ion (OH). For the reference state a defect as far away from both grain boundaries in the supercell as possible has been chosen. It is assumed to correspond to a defect in the grain interior.

When a charged defect such as an oxygen vacancy is introduced into a supercell, the use of periodic boundary conditions results in an effective lattice of charged defects which interact with each other. The electrostatic interaction is long-ranged and causes an error in the calculated total energy. However, the defect segregation energy is defined as the difference between the formation energy of a defect at an arbitrary site in the cell and the formation energy of a defect at a reference site. As both formation energies are calculated for cells of the exact same size and shape, the errors due to defect interactions can be expected to cancel to a large extent.

In the calculation of vacancy segregation energies we have compared total energies both before and after structural relaxation of the cells. Resulting segregation energies for each plane can be seen in Figures 6-8. Commencing with the $(111)[\bar{1}10]$ grain boundary, there are six oxygen sites in each even plane and zero oxygen sites in the odd planes. In the even planes four of the sites have one segregation energy and two sites have another, leading to two different segregation energies per plane. As can be seen in Figure 6 the oxygen sites in

the grain boundary plane, plane zero, have the lowest segregation energies (−0.51 and −0.54 eV) while the sites in the next layer have significantly higher energies. Further away from the grain boundary the segregation energy is close to zero.

The (112)[$\bar{1}$10] grain boundary has one site in each even plane and two sites with the same segregation energy in each odd plane, leading to one segregation energy per plane. The oxygen sites in plane one have the lowest vacancy segregation energy, −1.46 eV, as can be seen in Figure 7. In the grain boundary plane itself the segregation energy is quite high, whereas plane two, three and four have moderately low segregation energies (−0.5 to −0.3 eV). The difference between the unrelaxed and relaxed segregation energy in plane 1 indicates that significant lattice relaxation takes place around a vacancy in this plane, as has been previously observed [20].

Finally, the (210)[001] grain boundary has a somewhat different vacancy segregation energy curve (Figure 8). This grain boundary has two oxygen sites with different energies in each even plane and one site in each odd plane. The lowest vacancy segregation energy is found in plane four, −0.47 eV. However, the segregation energy in plane one is almost equally low, −0.45 eV. The other site type of plane four has the highest segregation energy of the boundary, 0.91 eV.

Segregation energies of the hydroxide ion (the proton) have been calculated for a number of oxygen sites close to the grain boundary plane. The energy of a hydroxide defect may depend on the orientation of the proton with regard to the oxygen ion. Favourable proton positions in bulk have been determined in previous work [31]. However, the reduced symmetry in the grain boundary will most likely favor other proton orientations. For each oxygen site we have therefore considered several different starting positions of the proton and performed an ionic relaxation for each case. Of the resulting configurations the one with the lowest energy is used for determining the segregation energy. Results can be seen in Table 3 along with relaxed and unrelaxed vacancy segregation energies. In all three grain boundaries the lowest proton segregation energy is around −0.8 eV. For the (112)[$\bar{1}$10] grain boundary the lowest proton segregation energy is higher than the lowest vacancy segregation energy, while the opposite holds for the other two boundaries. Also, in the (112)[$\bar{1}$10] and (111) [$\bar{1}$10] grain boundaries the same site has the lowest segregation energy for both defects, whereas this correlation is somewhat less pronounced for the (210)[001] boundary. The tendency of oxygen vacancies and protons to show increased stability at the same sites has previously been observed in DFT modelling of protonated oxides [34-36].

4.2   Space charge calculations

The calculated segregation energies have been used as input in the space charge model, with the goal of obtaining concentration profiles and potential barriers for each grain boundary. We define the grain boundary core for each grain boundary based on the vacancy segregation energies. In the case of the (111)[$\bar{1}$10] GB, the core will include plane zero and two as these planes contain sites with segregation energies substantially different from the reference state. This corresponds to a core width of $2z_c$=7.4 Å. For the (112)[$\bar{1}$10] GB planes zero to four are included giving a core width of $2z_c$=8.7 Å. Regarding the (210)[001] GB we also consider planes zero to four, giving a core width of $2z_c$=9.5 Å. Note that we have neglected the relatively small grain boundary expansion (cf. Table 2) in determining the core widths.

Figures 9-11 display the spatial variation of the electrostatic potential and site concentrations for temperatures of 600, 900 and 1200 K. At these temperatures the bulk material is fully protonated, half protonated and slightly protonated, respectively (cf. Figure 5). Variations in concentration within the core have been replaced with an average over the entire core for the sake of clarity. For all grain boundaries the positive defects aggregate in the grain boundary core and are depleted in the regions directly adjacent to it, the space charge layers. The core charge per unit area as a function of temperature can be seen in Figure 12, along with the concentration of vacancies and protons in the grain boundary core. For two of the GBs, (111)[$\bar{1}$10] and (210) [001], the protons give the dominant contribution to the positive core charge at all relevant temperatures (T=1600 K and below). In the (112)[$\bar{1}$10] GB the protons start to dominate below 700 K while at higher temperatures oxygen vacancies are more abundant. The core charge decreases with increasing temperature in all GBs, but the decline is steeper in the (111)[$\bar{1}$10] and (210)[001] GBs. The electrostatic potential barrier shows the same kind of temperature dependence as the core charge, as can be seen in Figure 13 (wet case).

The results of the space charge calculations show marked differences between the (112)[$\bar{1}$10] GB, in which the vacancy segregation energy is more negative than the hydroxide ion segregation energy, and the (111)[$\bar{1}$10] and (210)[001] GBs in which the relationship between the segregation energies is the opposite. As the proton concentration in bulk decreases with increasing temperature, vacancies move into the (112)[$\bar{1}$10] GB due to the strongly negative segregation energies. This keeps the core charge and potential barrier high and approximately constant. In the other two grain boundaries the core charge is mainly determined by the hydroxide ions as the vacances do not segregate strongly enough, leading to a more pronounced temperature dependence.

At temperatures relevant to experimental measurements (about 400 to 900 K) the calculated barrier heights range from 0.7 to 0.4 V, in agreement with experimental results [6,14,15,17] from materials with the same dopant concentration. For the (112)[$\bar{1}$10] GB the barrier height is essentially constant and equal to 0.6 V in the temperature range 400 to 900 K, while for the other two GBs the barrier height decreases with abound 0.2 V in

the same temperature range. Theoretical work by De Souza et al. [16] predicts that the potential barrier should be considerably lower in case of a high proton concentration in the core, contrary to what is seen here. They consider grain boundary cores where essentially all anion sites with favourable segregation energies are occupied by either vacanices or protons, so that replacement of vacancies by protons reduces the core charge. In our case, the density of sites with favourable segregation energies in the core is larger compared to De Souza et al. [16] and the grain boundary core is not saturated with defects. A proton-dominated core can therefore contain a larger total number of defects than a vacancy-dominated core, keeping the core charge and potential high.

In the hydrated material both vacancies and protons contribute to the core charge and potential barrier. To further investigate the effect of the two different defects on the GB properites the potential barrier has also been calculated for a dry material, completely devoid of protons. Figure 13 shows the height of the potential barrier ($\Delta\varphi(0)$) under hydrated and dry conditions as a function of temperature for all three grain boundaries. For the $(112)[\bar{1}10]$ GB, the one with the most energetically stable core oxygen vacancies, the potential barrier for the hydrated and dry case are very similar. For the other two grain boundaries, which have less stable core vacancies, the barrier under dry conditions is much lower compared to the wet case.

We can now compare our results to experimental findings. Shirpour et al. [19] conclude that the space charge potential does not differ significantly between wet and dry conditions. We find the same behaviour for the (112) $[\bar{1}10]$ GB. On the other hand, Kjølseth et al. [15] obtained a difference in the potential barrier under dry and wet conditions. They found that the barrier was substantially lower in the dry case and argued that the higher barrier in the wet case could be due to grain boundary core hydration, i.e. it is favourable for the protons to settle in the grain boundary core. Their results strongly resemble our results for the $(111)[\bar{1}10]$ and $(210)[001]$ GBs. However, the analysis by Kjølseth et al. was based on that the conductivity in the dry case was dominated by oxygen vacancies. If they instead assumed [15] that the conductivity was dominated by electron holes (which most likely is the case [37,38]) the barrier was increased by a factor of two, but still lower than in the wet case by about 0.1 V. A slight increase of the space charge potential upon hydration has also been suggested for acceptor-doped ceria, to explain a decrease of the grain boundary conductivity [39]. Similarly, it has been inferred that hydration increases the core charge in $BaZr_{0.7}Pr_{0.2}Y_{0.1}O_{3-\delta}$[40].

The magnitude and relation between the vacancy and proton segregation energies are essential for the behaviour of the potential barrier. For two of the GBs we find a fairly small tendency for vacancy segregation, with a segregation energy of about -0.5 eV. In another computational study [41], we have determined the vacancy segregation energy for a larger set of tilt grain boundaries using interatomic potentials of the rigid ion type. Most segregation energies are found to be in the range -2.0 to -1.0 eV. If these values for the vacancy segregation energy are more representative and if the proton segregation energy found here (about -0.8 eV) is typical, our result for the $(112)[\bar{1}10]$ GB should more accurately represent the actual behaviour of grain boundaries in barium zirconate.

5 Conclusions

Three tilt grain boundaries (GBs) in $BaZrO_3$ have been studied using density functional theory (DFT), and segregation energies of both oxygen vacancies and protons in the GB region have been determined. Both oxygen vacancies and protons tend to segregate to all three considered GBs. For at least two of the GBs, $(111)[\bar{1}10]$ and $(210)[001]$, it is clear that the stability of protons is increased on oxygen sites where vacancies are also more stable. This correlation has previously been seen in DFT modelling of protonated oxides [34-36]. The largest tendency for segregation is given by the lowest value of the site segregation energy in each GB. For oxygen vacancies the minimum segregation energy was found to be -0.5 eV for two of the GBs, $(111)[\bar{1}10]$ and (210) $[001]$, and -1.5 eV for the third one, $(112)[\bar{1}10]$. In the case of protons the minimum segregation energy was similar for all GBs, about -0.8 eV.

A layer-by-layer space charge model has been applied to determine the potential barrier and core charge resulting from defect segregation. In the space charge modelling, the charge compensating dopant ions have been assumed to be immobile and evenly distributed with a concentration corresponding to 10% of the Zr ions being replaced by trivalent dopant ions. Electrostatic barrier heights around 0.6 V were obtained in the temperature range 400 to 600 K for all GBs, and the calculated core charges were close to 0.7 Cm^{-2}. A barrier height of 0.6 V compares well with experimental data [6,14,15,17].

All three GBs became hydrated when the temperature is lowered. For two of the GBs, $(111)[\bar{1}10]$ and (210) $[001]$, protons gave the dominant contribution to the core charge at all relevant temperatures, while for the (112) $[\bar{1}10]$ GB oxygen vacancies dominate above 800 K. This temperature dependence follows from the relative magnitude of the oxygen vacancy and proton segregation energies.

Comparing the potential barrier obtained under hydrated and dry conditions it is seen that the barrier remains the same in the $(112)[\bar{1}10]$ GB, the GB with the largest tendency for vacancy segregation. This is in line with the conclusion in Ref. [19], that the space charge potential does not differ significantly between wet and dry conditions. In the other two GBs the barrier is lower under dry conditions than under hydrated conditions by about 0.4 V.

For two of the GBs we find fairly small tendencies to oxygen vacancy segregation, with segregation energies around −0.5 eV. In investigations of a larger set of tilt GBs in BaZrO$_3$ using interatomic potentials of the rigid ion type, segregation energies in the range −2.0 eV to −1.0 eV are found to be more typical [41]. If these energies are representative of GBs in BaZrO$_3$ and if the proton segregation energies found here are typical, the behaviour we obtain for the (112)[$\bar{1}$10] GB should more closely represent the actual behaviour of GBs in BaZrO$_3$.

In conclusion, not only segregation of oxygen vacancies but also segregation of protons is important for the formation of space charges in grain boundaries of hydrated barium zirconate. In some situations the protons may even be the primary source of excess charge in the grain boundary core.

Acknowledgements

List of Symbols
Latin letters
A	Area / m^2
c	Concentration per formula unit
e	Elementary charge / Colomb
E	Energy / eV
G	Gibb's free energy / eV
H	Enthalpy / eV
H	Hydrogen
k_B	Boltzmann's constant / eV K^{-1}
K	Equilibrium constant
N	Number of defects
O	Oxygen
p	Partial pressure / bar
P	Concentration per site, probability
S	Entropy / eV K^{-1}
T	Temperature / K
V	Volume / m^3
V	Vacancy
z	Coordinate

Greek letters
γ	Grain boundary energy / Jm^{-2}
Δ	Difference, grain boundary expansion / Å
ε	Dielectric permittivity / Fm^{-1}, relative dielectric constant
κ	Water partial pressure times equilibrium constant
μ	Chemical potential / eV
ρ	Charge density / Cm^{-3}
φ	Electrostatic potential / V

Super scripts
.	Positive defect charge
core	Grain boundary core
gi	Grain interior
i	Index
×	Neutral defect

Sub scripts
0	Standard
A	Acceptor dopant
D	Defect
H$_2$O	Water
hydr	Hydration
L	Layer
O	Oxygen
OH	Hydroxide ion
r	Relative
V	Vacancy

References

[1] K. D. Kreuer, *Annu. Rev. Mater. Res.* **2003**, *33*, 333.

[2] T. Ishihara (ed.), *Perovskite oxide for solid oxide fuel cells*, Springer, Dordrecht, **2009**,

[3] E. Fabbri, L. Bi, D. Pergolesi, E. Traversa, *Adv. Mater.* **2011**, *24*, 16517.

[4] K. D. Kreuer, *Solid State Ionics* **1999**, *125*, 285.

[5] H. G. Bohn, T. Schober, *J. Am. Ceram. Soc.* **2000**, *83*, 768.

[6] S. B. C. Duval, P. Holtappels, U. F. Vogt, E. Pomjakushina, K. Conder, U. Stimming, T. Graule, *Solid State Ionics* **2007**, *178*, 1437.

[7] P. Babilo, T. Uda, S. M. Haile, *J. Mater. Res.* **2007**, *22*, 1322.

[8] Y. Yamasaki, R. Hernandez-Sanchez, S. M. Haile, *Chem. Mater.* **2009**, *21*, 2755.

[9] H. J. Park, C. Kwak, K. H. Lee, S. M. Lee, E. S. Lee, *J. Eur. Ceram. Soc.* **2009**, *29*, 2429.

[10] S. P. S. Badwal, *Solid State Ionics* **1995**, *76*, 67.

[11] X. Guo, R. Waser, *Progr. Mater. Sci.* **2006**, *51*, 151.

[12] P. I. Dahl, H. L. Lein, Y. Yu, J. Tolchard, T. Grande, M. Einarsrud, C. Kjølseth, T. Norby, R. Haugsrud, *Solid State Ionics* **2011**, *182*, 32.

[13] F. Iguchi, T. Tsurui, N. Sata, Y. Nagao, H. Yugami, *Solid State Ionics* **2009**, *180*, 563.

[14] F. Iguchi, N. Sata, H. Yugami, *J. Mater. Chem.* **2010**, *20*, 6265.

[15] C. Kjølseth, H. Fjeld, Ø. Prytz, P. I. Dahl, C. Estournès, R. Haugsrud, T. Norby, *Solid State Ionics* **2010**, *181*, 268.

[16] R. A. De Souza, Z. A. Munir, S. Kim, M. Martin, *Solid State Ionics* **2011**, *196*, 1.

[17] C. Chen, C. E. Danel, S. Kim, *J. Mater. Chem.* **2011**, *21*, 5435.

[18] F. Iguchi, C. Chen, H. Yugami, S. Kim, *J. Mater. Chem.* **2011**, *21*, 16517.

[19] M. Shirpour, R. Merkle, J. Maier, *Solid State Ionics*, doi:10.1016/j.ssi.2011.09.006.

[20] B. J. Nyman, E. E. Helgee, G. Wahnström, *Appl. Phys. Lett* **2012**, *100*, 061903.

[21] M. Shirpour, B. Rahmati, W. Sigle, P. A. van Aken, R. Merkle, J. Maier, *J. Phys. Chem. C* **2012**, *116*, 2453.

[22] M. Shirpour, R. Merkle, C. T. Lin, J. Maier, *Phys. Chem. Chem. Phys.* **2012**, *14*, 730.

[23] J. Maier, *Progr. Solid State Chem.* **1995**, *23*, 171.

[24] R. A. De Souza, *Phys. Chem. Chem. Phys.* **2009**, *11*, 9939.

[25] A. C. T. van Duin, B. V. Merinov, S. S. Han, C. O. Dorso, W. A. Goddard III, *J. Phys. Chem. A* **2008**, *112*, 11414.

[26] G. Kresse, J. Hafner, *Phys. Rev. B.* **1993**, *48*, 13115.

[27] G. Kresse, J. Furthmüller, *Phys. Rev. B.* **1996**, *54*, 11169.

[28] J. Perdew, K. Burke, M. Ernzerhof, *Phys. Rev. Lett.* **1996**, *77*, 3865.

[29] P. Blöchl, *Phys. Rev. B.* **1994**, *50*, 17953.

[30] P. G. Sundell, M. E. Björketun, G. Wahnström, *Phys. Rev. B.* **2006**, *73*, 104112.

[31] M. E. Björketun, P. G. Sundell, G. Wahnström, *Faraday Discuss.* **2007**, *134*, 247.

[32] W . H. Press, S . A. Teukolsky, W . T. Vetterling , B . P. Flannery, *Numerical recipes*, Cambridge University Press, New York, USA, **2007**,

[33] E. E. Helgee, A. Lindman, B. J. Nyman, G. Wahnström, (in preparation).

[34] T. S. Bjørheim, A. Kuwabara, I. Ahmed, R. Haugsrud, S. Stølen, T. Norby, *Solid State Ionics* **2010**, *181*, 130.

[35] M. E. Björketun, C. S. Knee, B. J. Nyman, G. Wahnström, *Solid State Ionics* **2008**, *178*, 1642.

[36] B. J. Nyman, M. E. Björketun, G. Wahnström, *Solid State Ionics* **2011**, *189*, 19.

[37] K. Nomura, H. Kageyama, *Solid State Ionics* **2007**, *178*, 661.

[38] M. Shirpour, *Ph.D. Thesis*, University of Stuttgart, Stuttgart, Germany, **2011**, http://elib.uni-stuttgart.de/opus/volltexte/2011/6277.

[39] W. C. Chuech, C. Yang, C. M. Garland, W. Lai, S. M. Haile, *Phys. Chem. Chem. Phys.* **2011**, *13*, 6442.

[40] K. Kostøl Bakkemo, A. Maragasó, T. Norby, *Int. J. Hydrogen Energy* **2012**, *37*, 7970.

[41] A. Lindman, E. E. Helgee, B. J. Nyman, G. Wahnström, *Solid State Ionics*, (submitted).

Tables

Table 1 Supercells for DFT calculations: Axes, number of atoms, dimensions, grain boundary separation and tilt angle 2θ. a_0=4.25 Å is the lattice parameter.

GB	Axes	# of atoms	Dimensions	Separation / Å	2θ / degrees
(111)[$\bar{1}$10]	[11$\bar{2}$],[$\bar{1}$10],[111]	240	$\sqrt{6}a_0 \times 2\sqrt{2}a_0 \times 4\sqrt{3}a_0$	14.72	109.47
(112)[$\bar{1}$10]	[11$\bar{1}$],[$\bar{1}$10],[112]	180	$\sqrt{3}a_0 \times 2\sqrt{2}a_0 \times 3\sqrt{6}a_0$	15.62	70.53
(210)[001]	[$\bar{1}$20],[001],[210]	300	$\sqrt{5}a_0 \times 3a_0 \times 4\sqrt{5}a_0$	19.01	53.24
		200	$\sqrt{5}a_0 \times 2a_0 \times 4\sqrt{5}a_0$		

Table 2: Grain boundary expansion Δ_{gb} and energy γ_{gb}.

GB	Δ_{gb} / Å	γ_{gb} / Jm^{-2}
(111)[$\bar{1}$10]	0.20	0.51
(112)[$\bar{1}$10]	0.14	0.78
(210)[001]	0.26	1.14

Table 3 Vacancy segregation energies ΔE_V (unrelaxed and relaxed) and protons segregation energies ΔE_{OH}.

GB	Plane	ΔE_V (unrel) /eV	ΔE_V (rel) / eV	ΔE_{OH} / eV
(111)[$\bar{1}$10]	0	−0.31	−0.51	−0.79
	0	−0.30	−0.54	−0.80
	2	0.16	0.36	0.16
	2	0.17	0.42	0.31
(112)[$\bar{1}$10]	0	0.16	0.45	−0.02
	1	−0.61	−1.46	−0.75
	2	−0.13	−0.50	−0.28
	3	−0.17	−0.29	−0.20
	4	−0.45	−0.52	0.05
(210)[001]	0	0.26	0.39	−0.59
	0	0.18	−0.06	−0.38
	1	−0.12	−0.45	−0.75
	2	−0.17	−0.29	−0.43
	2	−0.03	0.05	−0.62
	3	−0.06	0.00	−0.33
	4	−0.33	−0.47	−0.36
	4	0.34	0.91	0.34

Figures
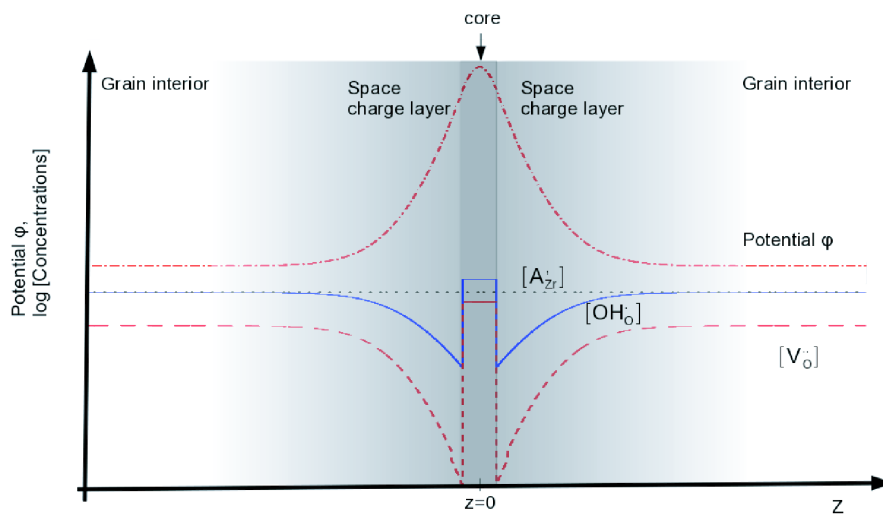
Fig. 1   Schematic of a grain boundary according to the space charge model.
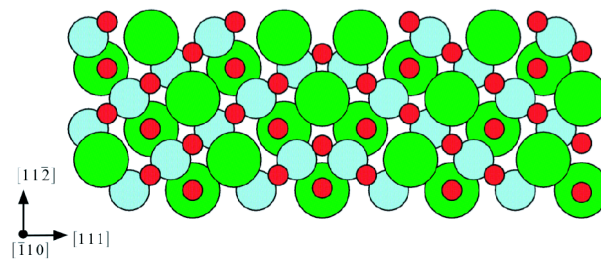
Fig. 2   The (111)[$\bar{1}$10] GB. Green stands for barium, blue for zirconium and red for oxygen.
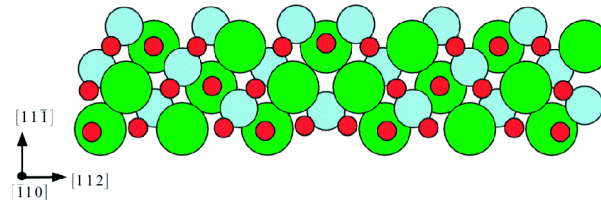
Fig. 3   The (112)[$\bar{1}$10] GB. Colors as in Figure 2.
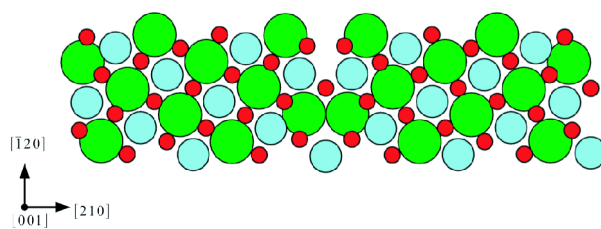
Fig. 4   The (210)[001] GB. Colors as in Figure 2.
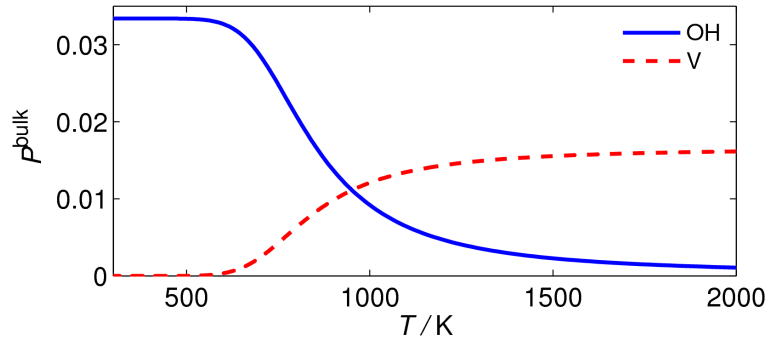
Fig. 5   Vacancy and hydroxide ion concentration per site in bulk.
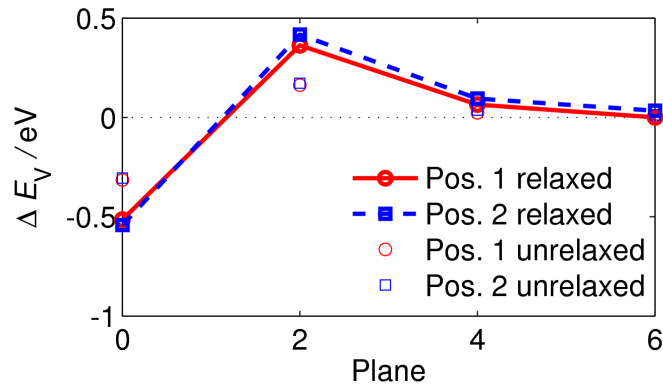
Fig. 6   Vacancy segregation energies near the $(111)[\bar{1}10]$ GB. The red solid line stands for oxygen position 1 and the dashed blue line for oxygen position 2. Small markers correspond to the unrelaxed case.
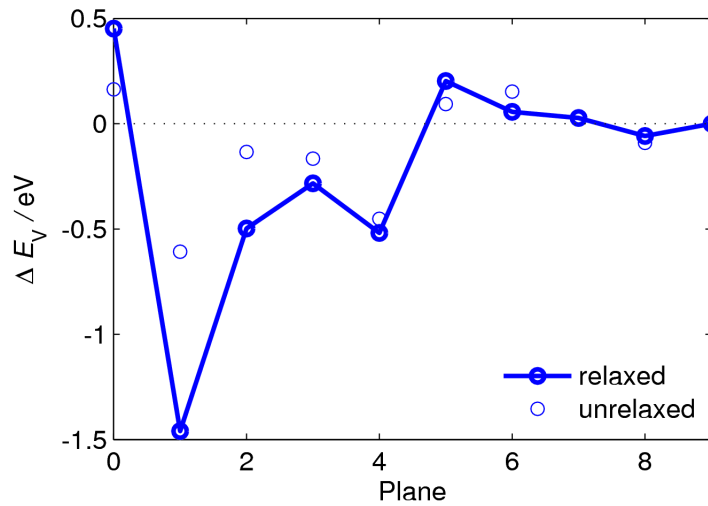
Fig. 7   Vacancy segregation energies close to the $(112)[\bar{1}10]$ GB. Small markers corresponds to the unrelaxed case.
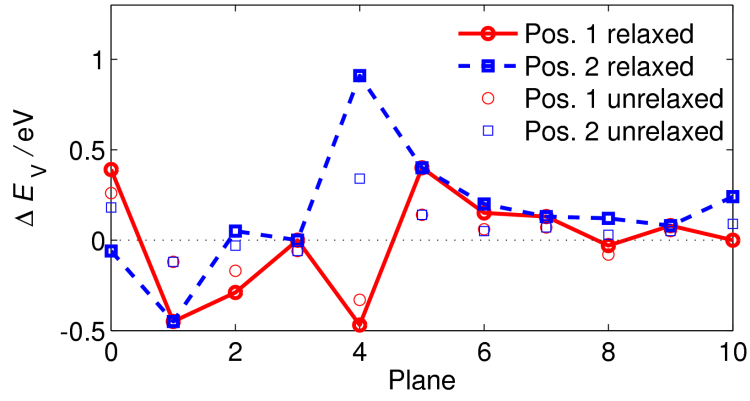
Fig. 8   Vacancy segregation energies close to the (210)[001] GB. The red solid line stands for oxygen position 1 and the dashed blue line for oxygen position 2. Small markers correspond to the unrelaxed case.
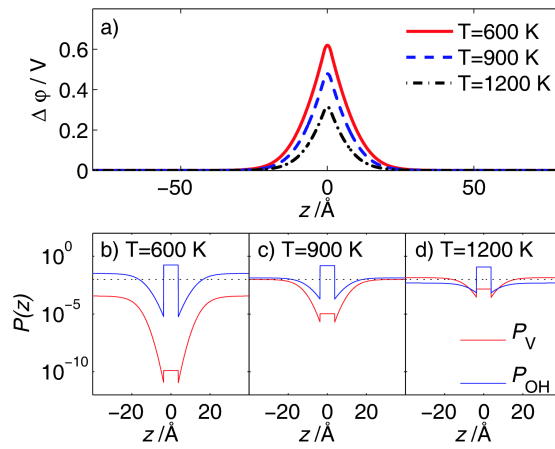
Fig. 9   Space charge results for the $(111)[\bar{1}10]$ GB, a) $\Delta\varphi$ (z) at 600, 900 and 1200 K, b)-d) P_V and P_{OH} at 600, 900 and 1200 K. Concentrations in the core region are set to an average value for the sake of clarity. The black dotted line at $P=0.01$ is a guide to the eye.
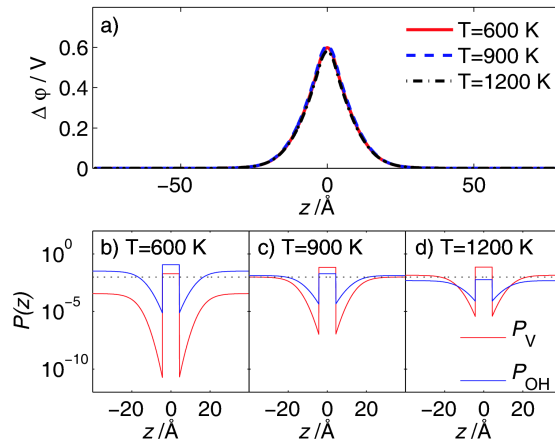
Fig. 10   Space charge results for the $(112)[\bar{1}10]$ GB, a) $\Delta\varphi$ (z) at 600, 900 and 1200 K, b)-d) P_V and P_{OH} at 600, 900 and 1200 K. Concentrations in the core region are set to an average value for the sake of clarity. The black dotted line at $P=0.01$ is a guide to the eye.
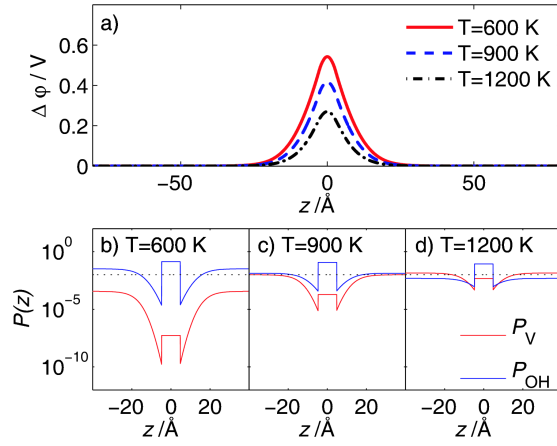
Fig. 11 Space charge results for the (210)[001] GB, a) $\Delta \varphi$ (z) at 600, 900 and 1200 K, b)-d) P_V and P_{OH} at 600, 900 and 1200 K. Concentrations in the core region are set to an average value for the sake of clarity. The black dotted line at P=0.01 is a guide to the eye.
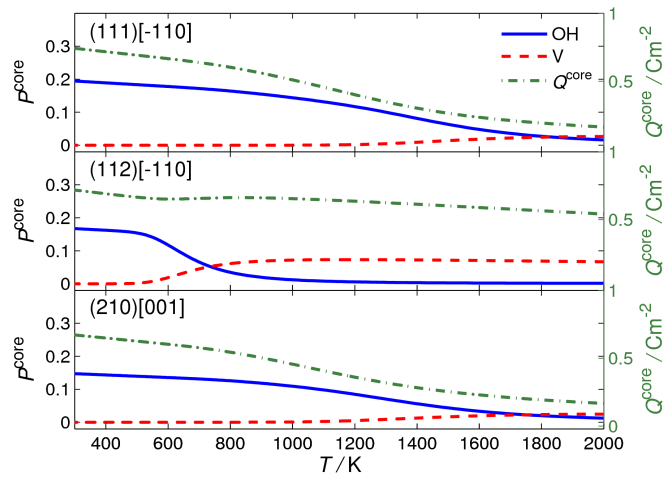
Fig. 12 Vacancy and hydroxide ion concentration per site in the core as a function of temperature, along with the total core charge. Top panel corresponds to the (111)[$\bar{1}$10] GB, middle panel to the (112)[$\bar{1}$10] GB and the bottom panel to the (210)[001] GB.
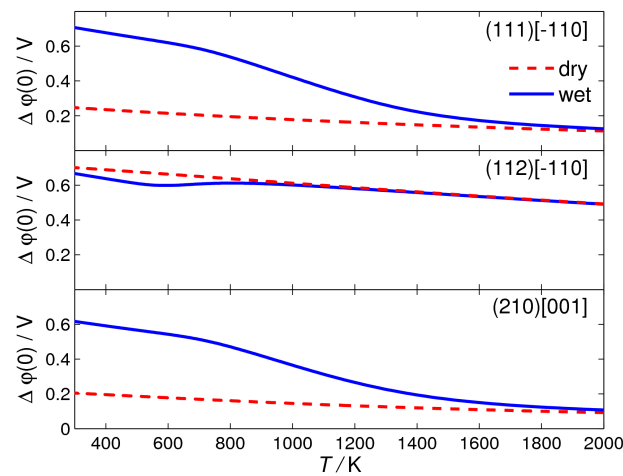
Fig. 13 Potential barrier height under dry and hydrated conditions as a function of temperature. Top panel corresponds to the (111)[$\bar{1}$10] GB, middle panel to the (112)[$\bar{1}$10] GB and the bottom panel to the (210)[001] GB.